Sensors and Open-Switch FDI of Induction Motor Drives based on Control Reconfiguration

Abstract

This paper presents a fault detection and isolation (FDI) strategy designed to enhance the reliability of induction motor drives by addressing both sensor faults and open-circuit (OC) faults in inverter switches. For sensor faults, the proposed approach employs control reconfiguration by combining estimates from an observer bank with measured stator current and mechanical speed signals. Faults are diagnosed by analyzing discrepancies between estimated and measured variables, and faulty sensor signals are replaced with reliable estimates to ensure continuous operation under fault conditions. With respect to OC faults, the FDI strategy involves averaging the phase current over a half-cycle and comparing it to a predefined threshold to diagnose both single and multiple OC faults in the inverter switches. The effectiveness of the proposed FDI strategy is validated through experimental tests conducted under various fault scenarios.

Keywords: Detection and Isolation, Electric drives, Induction Motor, Sensor Faults, Open-Switch Faults

1. Introduction

Induction motor drives (IMD) comprise a motor, an inverter, a controller, and sensors; and are highly valued for their low cost, robustness, reliability, and ease of maintenance. They are widely used across various sectors, including industrial applications such as pumps, compressors, fans, and crushers; commercial applications like elevators, escalators, and household appliances; as well as in electric vehicles and wind generators. To achieve high dynamic performance, IMD employ closed-loop control strategies that are programmed into the controller. These strategies rely on feedback information obtained from stator voltages, currents and mechanical speed sensors. Then the controller processes these feedback signals information, compares them with desired reference values, and generates control commands [1]. If any of these sensors fails, the information about the motor operating status reflected in the control will be erroneous, causing the algorithm to send incorrect switching signals to the inverter. This can lead to degraded control performance, equipment damage, or economic losses [2]. Sensors are susceptible to different types of faults, such as gain variations, offset errors, and disconnection [3]. From the perspective of the IMD, complete disconnection results in a total loss of feedback information to the control system, which can potentially lead to the shutdown of the equipment [4]. Therefore, since adding sensors is often costly or impractical, estimated values are used to maintain IMD operation [1, 2, 4].

The inverter includes power switching devices to adjust the shape and frequency of the output AC voltage, thereby regulating the torque and speed of the motor. Consequently, failures in power switching devices degrade the IMD performance, and are classified as short-circuit (SC) and open-circuit (OC) faults [5]. SC faults produce instantaneous over-currents, which can cause immediate damage to other components of the inverter. Therefore, ED include standard protection components that act quickly when these types of faults occur [6]. While OC faults place additional stress on healthy switches, they do not compromise the operation of the ED in the short term; however, they can lead to secondary faults in the inverter and potentially result in a shutdown over time [7].

The literature contains numerous studies on FDI strategies designed for specific types of faults, such as sensor faults [8, 9,10] or inverter switch OC faults [11]. However, integrating diagnostic methods for each fault type into a single FDI strategy may increase computational costs, introduce latency in fault detection, be impractical to implement, or lead to incorrect diagnoses due to the coupling of residuals and parameter uncertainties [12]. In recent years, significant efforts have been made to develop comprehensive FDI strategies that address both sensor faults and OC faults in inverter switches [13, 14, 15, 16, 17, 18, 19, 20, 21, 22, 23, 24, 25, 26, 27, 28, 29, 30]. In general, these FDI strategies can be classified in data driven-based, signal-based and model-based. Data driven-based strategies relies on

learning the relationship between fault types and their corresponding characteristics using historical data. For example in [13] a FDI is proposed based on online metric learning to diagnose OC faults in current sensors and inverter switches in permanent magnet synchronous motor drives (PMSMD). In [14], a strategy is proposed for the simultaneous diagnosis of open-circuit faults in IGBTs and current sensor faults in three-phase inverters. The method combines the Park transform with the fast Fourier transform to effectively extract fault features, and the diagnosis is subsequently carried out using a temporal convolutional neural network. Additionally, [15] introduces a FDI for current sensors and IGBTs in IMD, utilizing real-time data analysis to identify and classify faults in both types of components. Furthermore, [16] employs an enhanced regularized extreme learning machine to diagnose and distinguish OC faults in current sensors and switches in PMSMD. However, data-driven approaches require a substantial amount of historical test data to adequately train the algorithm, which makes their practical implementation challenging [31].

Signal-based methods utilize the measured signals to extract fault characteristics. In [17] an approach to detect, isolate, and discriminate current sensor disconnection faults and OC faults in power semiconductors of three-phase PMSMD is proposed. The proposed FDI strategy combines two fault indicators: the comparison of the average normalized product of two stator phase currents against fixed thresholds, and the polarity of the normalized average current. In [18] an algorithm is proposed for detecting multiple OC faults in IGBTs, as well as disconnections in the current and mechanical speed sensors of PMSMD. However, achieving the desired performance requires dynamically setting thresholds and low-pass filters with a variable cutoff frequency. It is also worth mentioning that this FDI strategy relies on the speed sensor to perform critical diagnostic calculations. Subsequently, [19] introduces a FDI strategy for three-phase four-wire inverters with physical sensor redundancy (additional voltage sensors), capable of diagnosing multiple OC faults in power switches and single disconnection faults in current sensors under nonlinear loads. This approach employs Fourier fitting to analyze and adjust the inverter's bridge voltage signals. Fault diagnosis is then performed using the normalized detection variables of the ideal bridge arm voltage and the fitted bridge arm voltage.

In model-based strategies, faults are generally identified using residuals computed from the differences between measured and estimated signals. In [20] a strategy based on the averaged model of the output line and phase voltages of a grid-tied three-phase inverter proposes single current sensor and OC switches FDI. In [21] a strategy for diagnosing and identifying a single OC faults in power switches and multiple current sensors fault for a matrix converter-based PMSMD with finite control set−model predictive control (FCS-MPC) is presented. Additionally, [22] introduces an open-loop observer-based FDI strategy for current sensors and inverter switches in traction IMD. This approach has proven effective for diagnosing gain faults and disconnections in current sensors, as well as single OC faults in inverter switches.

In [23] a FDI strategy is proposed for diagnosing multiple OC IGBTs and current sensor faults in PMSMD, based on residual generation using estimated and measured stator currents. Moreover, [24] presents a comprehensive strategy for the simultaneous diagnosis of IGBT OC and incipient faults in current sensors of PMSMD on electric vehicles, utilizing a sliding mode observer with an adaptive thresholds. Furthermore, [25] introduces a simultaneous diagnosis strategy for OC faults, as well as for gain, disconnections and offset faults in current sensors of three-level neutral-point-clamped (NPC) inverters connected to the grid. Subsequently, [26] proposes an FDI approach based on a reduced-order observer for grid-tied NPC inverters, and in [27], a similar approach is applied to IMD subjected to the same faults. It is important to highlight that the sensitivity and robustness of these methods [23, 24, 25, 26, 27] depend on a defined adaptive threshold.

In [28], a strategy is proposed for diagnosing OC faults in switches and current sensors, based on FCS-MPC for IMD. It is worth noting that only single faults are identified in both the current sensors and the inverter switches. Moreover, [29] presents a diagnostic strategy for doubly-fed induction generators that can handle IGBT faults, as well as rotor and stator current sensor outages and stator voltage sensor outages, utilizing an augmented state and disturbance observer. Additionally, [30] develops a comprehensive FDI strategy addressing speed sensor faults, voltage sensor faults, current sensor faults, open phase faults, and single switch OC faults in two-level VSI-fed dual three-phase PMSMD, utilizing sensor redundancy. However, the approach in [29, 30] has been demonstrated only for single faults. Scenarios involving multiple faults occurring over time, such as faults in multiple current sensors or inverter switches (cross faults or double-upper or lower faults), are not addressed.

On the other hand, in [32], a diagnostic method is pro-

posed that combines sliding-mode observers with current spectral analysis to detect sensor and motor faults. Depending on the type of fault, the method either replaces the measurements with estimates or changes the speed control strategy to sustain the operation of the IMD. However, although this approach addresses multiple components, it does not detect and isolate OC faults in the inverter switches.

Although the aforementioned FDI strategies reported in the literature have shown effectiveness in diagnosing faults across various components, there are still several aspects that warrant further attention, such as:

- The requirement of extensive historical data to train FDI algorithms.
- Dependence on hardware redundancy.
- Complex implementation or heavy computations make real-time deployment difficult.
- Relying exclusively on a single approach for fault diagnosis entails significant limitations. In signal-based methods, performance heavily depends on the availability and reliability of measurements, so a sensor failure may lead to the loss of critical information for control. On the other hand, model-based methods may result in incorrect diagnoses due to the coupling of residuals.
- Its effectiveness is not demonstrated in scenarios involving successive failures in multiple current sensors or OC faults.

To address these issues, this work proposes a unified, reconfigurable diagnosis and fault strategy that combines signal-based and model-based methods, enabling the management of multiple and successive sensor and switch faults. To do this, it uses only two stator current sensors and a mechanical speed sensor. In addition, the proposed strategy is composed of three main stages: control reconfiguration, signal processing, and FDI. The control reconfiguration stage includes a bank of observers that provides estimates of the stator currents and mechanical speed. In the event of a sensor failure, the corresponding measurement is replaced by its estimated value to keep the IMD operational. Faults are identified by monitoring the difference between the measured and estimated variables. If this deviation exceeds a predefined threshold, a logic signal is triggered.

Since the currents are measured at the inverter output, any switch fault may result in inaccurate estimates in the mathematical models, potentially causing false fault diagnoses in the sensors and leading to unnecessary control reconfiguration. To mitigate this, a separate signal processing stage is used, which relies on the average of the current signals to generate complementary logic indicators. Finally, in the FDI stage, the diagnosis is carried out by evaluating all the logic signals.

Experimental tests were conducted to evaluate the proposed strategy. The results demonstrate its practical effectiveness in diagnosing sensor and OC faults in IMD.

The rest of the work is organized as follows. In Section 2 the system under study is presented. In Section 3 the proposed FDI strategy is described. Finally, Section 4 presents the experimental validation of the proposed strategy.

2. System under study

An IMD with a field-oriented control (FOC) strategy is considered in this work, see Fig. 1. The FOC decouples the magnetic flux and torque, enabling their independent control to achieve a fast and accurate dynamic response. To make these variables independent, a transformation is applied, converting the measured currents, denoted by i_a and i_b, into the rotating reference frame dq through the Park transform

$$\begin{bmatrix} i_d \\ i_q \end{bmatrix} = \begin{bmatrix} \cos\hat{\rho} & \sin\hat{\rho} \\ -\sin\hat{\rho} & \cos\hat{\rho} \end{bmatrix} \begin{bmatrix} i_\alpha \\ i_\beta \end{bmatrix}, \tag{1}$$

where $\hat{\rho}$ represents the transformation angle; i_α and i_β are the currents in the stationary reference frame, which are obtained using the Clarke transform:

$$\begin{bmatrix} i_\alpha \\ i_\beta \end{bmatrix} = \begin{bmatrix} 1 & 0 \\ \frac{1}{\sqrt{3}} & \frac{2}{\sqrt{3}} \end{bmatrix} \begin{bmatrix} i_a \\ i_b \end{bmatrix}. \tag{2}$$

These currents are regulated with PI controllers, where the direct current reference, i_d^*, controls the magnetic flux (typically constant or slowly varying) and the quadrature current reference i_q^* controls the torque produced by the motor [33]. The outputs of the PI controllers are used to set the reference voltages, $\mathbf{u}_{\alpha\beta}^*$, in the SVPWM. The considered IM model consists of an electrical subsystem and a mechanical subsystem. The electrical subsystem is described in a stationary reference frame as:

$$\begin{aligned} \dot{\mathbf{x}} &= \mathbf{A}(\omega_m)\,\mathbf{x} + \mathbf{B}\,\mathbf{u}_{\alpha\beta} \\ \mathbf{y} &= \mathbf{C}\,\mathbf{x} \end{aligned} \tag{3}$$

where

$$\mathbf{A}(\omega_m) = \begin{bmatrix} -a & 0 & bc & b\omega_m \\ 0 & -a & -b\omega_m & bc \\ L_m c & 0 & -c & -\omega_m \\ 0 & L_m c & \omega_m & -c \end{bmatrix};$$

$$\mathbf{B} = \begin{bmatrix} d & 0 \\ 0 & d \\ 0 & 0 \\ 0 & 0 \end{bmatrix}; \quad \mathbf{C} = \begin{bmatrix} 1 & 0 & 0 & 0 \\ 0 & 1 & 0 & 0 \end{bmatrix}; \tag{4}$$

and

$$a = \frac{1}{\sigma L_s}\left(R_s + \frac{L_m^2}{L_r^2}R_r\right); \quad b = \frac{L_m}{\sigma L_s L_r};$$
$$c = \frac{R_r}{L_r}; \quad d = \frac{1}{\sigma L_s}; \quad \sigma = 1 - \frac{L_m^2}{L_s L_r}.$$

Here, $\mathbf{x} = \left[i_\alpha,\, i_\beta,\, \lambda_\alpha,\, \lambda_\beta\right]^T$ represents stator currents and rotor fluxes; $\mathbf{y} = \left[i_\alpha,\, i_\beta\right]^T$ represents the measured currents; $\mathbf{u}_{\alpha\beta} = \left[u_\alpha,\, u_\beta\right]^T$ represents the stator voltages; ω_m represents the mechanical speed; R_s, R_r, L_s, L_r represent the stator and rotor resistances and inductances stator and rotor, respectively; and L_m represents the mutual inductance. In addition, the mechanical subsystem is described as:

$$\dot{\omega}_m = \frac{P}{2J}\left(T_m - T_L\right) \tag{5}$$
$$T_m = \frac{3}{2}\frac{P}{2}\frac{L_m}{L_r}\left[\lambda_\alpha i_\beta - \lambda_\beta i_\alpha\right]$$

where J represents the rotor inertia; P represents the number of poles; T_m and T_L represent the motor and load torque, respectively.

Speed and current sensor measurements are considered prone to faults. Additive arbitrary signals are used to model these faults, as follows:

$$\omega_m = \omega_{m0} + m_\omega, \quad i_a = i_{a0} + m_a, \quad i_b = i_{b0} + m_b \tag{6}$$

where ω_{m0} is the rotor speed; i_{a0} and i_{b0} are the stator currents; m_ω, m_a, and m_b are arbitrary signals representing the faults. Note that this fault modeling approach can represent both constant and time-varying faults; therefore, different kinds of faults can be considered, such as offset, noise, gain, or constant feedback [3]. In this work, only disconnection (null output) faults are considered, i.e., the fault signal cancels the measurement.

3. Proposed strategy

As shown in Fig. 1, the proposed strategy consists of a control reconfiguration stage, a sensor residual post-processing stage, a current signal post-processing stage, and a FDI stage. The control reconfiguration stage consists of an observer bank that estimates the stator currents and mechanical speed, see Fig. 2. These estimates are utilized to reconfigure the control when the logic signals $\mathbf{F}_x = \left[F_{i_a},\, F_{i_b},\, F_\omega\right]^T$, generated in sensor residual post-processing stage are activated. To keep the IMD running when sensor faults occur, the affected measurements are replaced by their corresponding estimations by the control reconfiguration. In parallel, the current sensors signals processing stage generates signals sensitive to OC faults. Finally, from Fig. 1 it can be observed that the FDI is obtained based on the signals $\mathbf{F}_x$ and $\mathbf{F}_{jk}$ generated by sensor residual post-processing and current signal post-processing stage, respectively. In summary, the proposed strategy takes as inputs the reference voltages $\mathbf{u}^*_{\alpha\beta} = \left[u^*_\alpha, u^*_\beta\right]^T$, the stator current measurements $\mathbf{i}_{ab} = \left[i_a, i_b\right]^T$, and the mechanical speed measurement ω_m. Based on these signals, the strategy provides the estimation of the rotor flux position $\hat{\rho}$, the proposed phase currents $\mathbf{i}'_{ab} = \left[i'_a,\, i'_b\right]^T$, and the proposed mechanical speed ω'_m. It is important to note that the proposed variables $\mathbf{i}'_{ab}$ and ω'_m may either be measurements or estimates from state observers, depending on the control reconfiguration decision.

3.1. Observer bank

Sensor fault detection and control reconfiguration rely on estimates of stator currents and mechanical speed. These estimates are generated by a bank of observers integrated into the control reconfiguration stage (see Fig. 2). This bank consists of observers denoted O_c and O_s, where the subscripts c and s refer to currents estimation and speed estimation, respectively. The observer O_c generates the phase currents estimations, $\hat{i}_a$ and $\hat{i}_b$, as well as the rotor flux position estimation, $\hat{\rho}_1$. In addition, O_s generates the speed $\hat{\omega}_m$ and an additional estimation of the rotor flux position $\hat{\rho}_2$. These observers are based on IM model (3) and are described as follows:

$$O_c \left\{ \dot{\hat{\mathbf{x}}}_c = \mathbf{A}_c\left(\omega_m\right)\hat{\mathbf{x}}_c + \mathbf{B}\mathbf{u}^*_{\alpha\beta} \right. \tag{7}$$
$$O_s \left\{ \dot{\hat{\mathbf{x}}}_s = \mathbf{A}_s\left(\hat{\omega}_m\right)\hat{\mathbf{x}}_s + \mathbf{B}\mathbf{u}^*_{\alpha\beta} \right. \tag{8}$$

where

$$\mathbf{A}_c(\omega_m) = \begin{bmatrix} -a & 0 & bc & b\omega_m \\ 0 & -a & -b\omega_m & bc \\ L_m c & 0 & -c & -\omega_m \\ 0 & L_m c & \omega_m & -c \end{bmatrix} \tag{9}$$

$$\mathbf{A}_s(\hat{\omega}_m) = \begin{bmatrix} -a & 0 & bc & b\hat{\omega}_m \\ 0 & -a & -b\hat{\omega}_m & bc \\ L_m c & 0 & -c & -\hat{\omega}_m \\ 0 & L_m c & \hat{\omega}_m & -c \end{bmatrix} \tag{10}$$

The vectors of stator currents and rotor flux linkages used in the current and speed estimation ob-

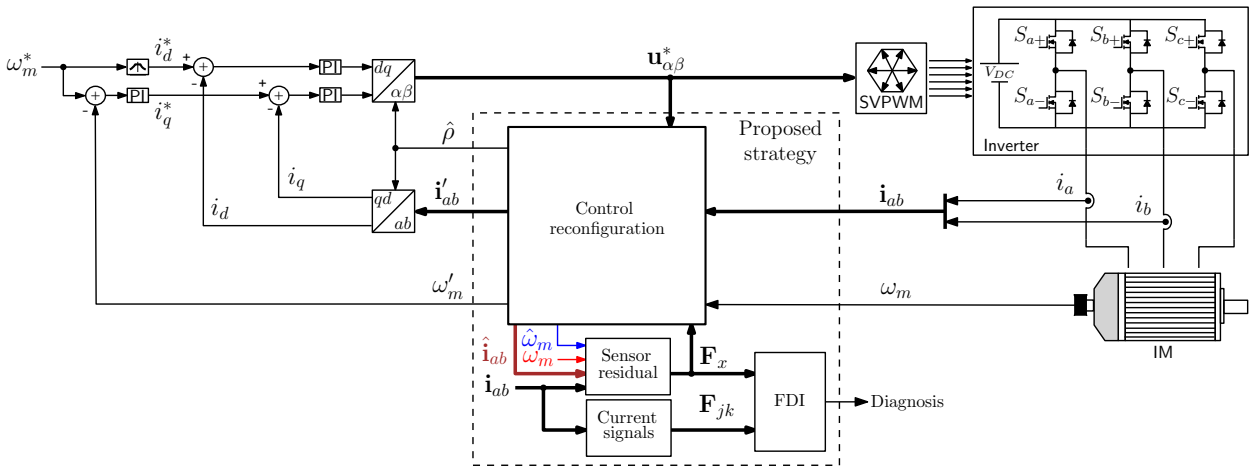

Figure 1: Induction motor drive with Proposed strategy.

servers are given by $\hat{\mathbf{x}}_c = \left[\hat{i}_{\alpha c}, \hat{i}_{\beta c}, \hat{\lambda}_{\alpha c}, \hat{\lambda}_{\beta c}\right]^T$ and $\hat{\mathbf{x}}_s = \left[\hat{i}_{\alpha s}, \hat{i}_{\beta s}, \hat{\lambda}_{\alpha s}, \hat{\lambda}_{\beta s}\right]^T$.

The estimated phase currents are obtained as $\hat{i}_a$ and $\hat{i}_b$ from:

$$\begin{bmatrix} \hat{i}_a \\ \hat{i}_b \end{bmatrix} = \begin{bmatrix} 1 & 0 \\ -\frac{1}{2} & \frac{\sqrt{3}}{2} \end{bmatrix} \begin{bmatrix} \hat{i}_{\alpha c} \\ \hat{i}_{\beta c} \end{bmatrix}. \tag{11}$$

Furthermore, rotor flux position is estimated from observers in (7) and (8) as $\hat{\rho}_1 = \text{atan2}\left(\hat{\lambda}_{\beta c}, \hat{\lambda}_{\alpha c}\right)$, and $\hat{\rho}_2 = \text{atan2}\left(\hat{\lambda}_{\beta s}, \hat{\lambda}_{\alpha s}\right)$.

The speed estimation is obtained from a sliding-mode injection term:

$$\hat{\omega}_m = K \text{ sign } (\hat{S}) \tag{12}$$

where K, is a positive gain sufficiently large to ensure the convergence of the observer and $\hat{S}$, represents the sliding surface of the speed observer defined as:

$$\hat{S} = \left(\hat{i}_{\beta s} - i_\beta\right)\hat{\lambda}_{\alpha s} - \left(\hat{i}_{\alpha s} - i_\alpha\right)\hat{\lambda}_{\beta s} \tag{13}$$

where

$$\begin{bmatrix} i_\alpha \\ i_\beta \end{bmatrix} = \frac{2}{3}\begin{bmatrix} 1 & -\frac{1}{2} \\ 0 & \frac{\sqrt{3}}{2} \end{bmatrix} \begin{bmatrix} i_a \\ i_b \end{bmatrix}. \tag{14}$$

Since $\hat{\omega}_m$ is a discontinuous signal, the speed observer employs a low-pass filter (LPF) to attenuate the high-frequency noise resulting from the estimation based on the switched signal. Although LPF applied to the estimated speed may introduce a phase lag, it does not compromise the primary objective, which is to diagnose faults in the speed sensor and, in the event of a fault, maintain continuous operation by replacing the measurement with the observer-based estimate. Future improvements could consider adaptive-gain strategies to further mitigate the filtering delay, as reported in [34].

It is worth mentioning that the two observers use different measurements. In the current observer O_c, the model is parameterized by the measured rotor speed ω_r and the reference voltages $\mathbf{u}^*_{\alpha\beta}$ and does not use measured stator currents in its feedback. Therefore, its error dynamics are $\dot{\mathbf{e}} = \mathbf{A}(\omega_r)\,\mathbf{e}$ and convergence relies on the electrical matrix $\mathbf{A}(\omega_r)$ being stable under standard physical conditions of IM ($R_s > 0$, $R_r > 0$, $L_m \neq 0$, $\sigma \neq 0$); the convergence and robustness under parameter variations are analyzed in [22].

In contrast, the sliding-mode speed observer O_s uses the measured stator currents i_α, i_β in its feedback law. For the corresponding output matrix $\mathbf{C}$, the pair $(\mathbf{A}, \mathbf{C})$ is observable under standard physical conditions of IM (the observability determinant reduces to a positive expression for $L_m \neq 0$ and $R_r > 0$). The SMO additionally relies on sliding assumptions (sufficient injection gain and rotor speed varying slowly relative to the electrical dynamics) to ensure the sliding condition and the extraction of the equivalent speed [34].

When a fault occurs, the faulty sensor readings are replaced by the corresponding estimates, ensuring continued operation under fault.

3.2. Control reconfiguration

The feedback signals used in the control loop depend on the logic state of the sensors signals $\mathbf{F}_x$. When any of these signals is activated, measurements coming from a sensor are replaced by its estimations, according to Table 1. When a failure of a phase sensor occurs, the

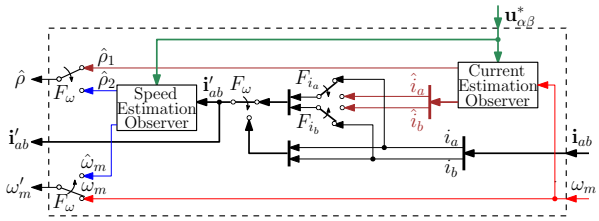

Figure 2: Control reconfiguration.

Table 1: Feedback based on sensors logic signals

F_{i_a}	F_{i_b}	F_ω	**Condition**	**Feedback**
0	0	0	Normal operation	$i_a, i_b, \hat{\rho}_1, \omega_m$
1	0	0	i_a fault	$\hat{i}_a, i_b, \hat{\rho}_1, \omega_m$
0	1	0	i_b fault	$i_a, \hat{i}_b, \hat{\rho}_1, \omega_m$
1	1	0	i_a and i_b fault	$\hat{i}_a, \hat{i}_b, \hat{\rho}_1, \omega_m$
X	X	1	ω_m fault	$i_a, i_b, \hat{\rho}_2, \hat{\omega}_m$

* X indicates "don't care" condition.

logic signal F_{i_a} is activated, and therefore this measurement is replaced by the estimate $\hat{i}_a$. Likewise, when b phase sensor fails, the logic signal F_{i_b} is activated, and i_b is replaced by $\hat{i}_b$. If both current sensors fail, the measurements are replaced by their corresponding estimates. In addition, when current sensor faults occur, the input measurements $\mathbf{i}_{ab}$ used by the speed estimation observer O_s (8), become incorrect. Therefore, they are replaced by the estimates provided by the current estimation observer O_c (7) in order to prevent the activation of F_ω and, consequently, an incorrect reconfiguration, see Table 1 and Fig. 2.

When the speed sensor is under fault, the estimation of the rotor flux position $\hat{\rho}_1$, generated by the observer O_c, becomes wrong. Therefore, is replaced by $\hat{\rho}_2$ corresponding to speed estimation observer. In addition, the measured speed ω_m is replaced by the estimated speed $\hat{\omega}_m$, see Table 1 and Fig. 2. The speed sensor fault also affects the estimations generated by the O_c observer may therefore trigger the logic signals F_{i_a} and F_{i_b}, leading to an incorrect reconfiguration. When F_ω is activated, the speed estimation observer is forced to use the current measurements (see Fig. 2). However, it may happen that the F_{i_a} and F_{i_b} signals are activated first because O_c also requires the speed sensor measurement. In this case, an incorrect reconfiguration will momentarily occur until the F_ω signal is activated due to the speed sensor fault.

3.3. Sensor residuals post-processing

The sensors residuals post-processing stage generates the residuals r'_ω, r'_{i_j}, where the subscript $j \in \{a, b\}$, in order to obtain the sensor fault detection logic signals F_ω, F_{i_j}, as can be seen in Fig. 3. First, the errors e_ω and e_{i_j} go through a normalization stage to make the FDI independent of the load torque applied to the IM. Specifically, e_ω is normalized by the reference speed ω^*_r, while e_{i_j} is normalized by $i_n = \sqrt{(i^*_d)^2 + (i^*_q)^2}$. Then, by taking the absolute value, the residuals $r_\omega = |e_\omega|$ and $r_{i_j} = \left|e_{i_j}\right|$ are obtained.

It should be noted that, assuming the observer does not exhibit any uncertainties or parametric variations, we may consider that $\hat{\omega}_m \approx \omega_{m0}$ and $\hat{i}_j \approx i_{j0}$. Under this assumption, from (6) it can be observed that, if a speed sensor-fault occurs, the speed residual satisfies $r_\omega \approx |m_\omega| / \omega^*_m$, while if a current-sensor fault is present in the i_j sensor, the current residual satisfies $r_{i_j} \approx \left|m_j\right| / i_n$. Therefore, the residuals are sensitive to the arbitrary fault signals [35].

The residuals previously obtained are subsequently passed through a saturation stage to limit their maximum values, using the norm of each signal as the bounding criterion. Subsequently, an asymmetrical slope limiter is used, allowing an unlimited rising rate while restricting the falling rate. The resulting post-processed residuals r'_ω and r'_{i_j} are then compared with the threshold levels ω_{th} and i_{th}, respectively. When residuals exceeded the threshold level, the sensor fault detection logic signals F_ω, F_{i_a} and F_{i_b} activate, indicating an alarm. It is worth mentioning that the threshold levels for ω_{th} and i_{th} were determined by varying speed, load torque, and parameters such as the stator and rotor resistances, and observing the maximum residuals under healthy conditions. Based on this information, a threshold level was chosen that is high enough to avoid false positives due to normal variations and noise, but low enough to immediately identify sensor disconnection faults [36, 35]. Although noise was not explicitly included in the mathematical formulation (3), the design of the thresholds implicitly accounts for the variance of the residuals induced by measurement noise, thereby ensuring the robustness of the proposed FDI strategy.

3.4. Current signals post-processing

The generation of switch logic signals is based on detecting intervals where some of the current half-cycles become zero. When a OC fault occurs in the S_{j+} switch, the positive half-cycle of the phase current j becomes zero. Similarly, if the fault occurs in the switch S_{j-}, the negative half-cycle of the phase current j is rendered

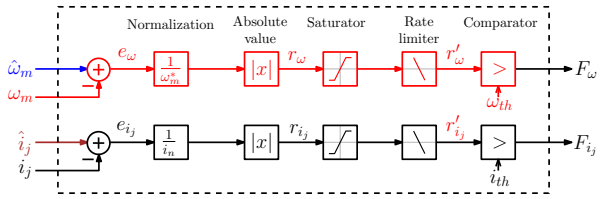

Figure 3: Sensor residuals post-processing stage.

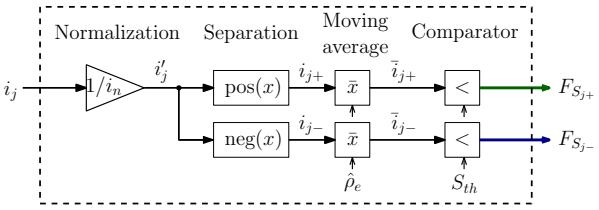

Figure 4: Current signals post-processing stage.

zero. In the case of a fault affecting an entire inverter leg (S_{j+} and S_{j-}), the current in phase j becomes completely zero. It should be noted that, in order to diagnose faults in the switches of phase c, the corresponding current is computed as $i_c = -(i_a + i_b)$ and subsequently processed at this step. The proposed current processing stage is described in Fig. 4. First, the phase currents i_j are normalized by i_n to make the signals independent of the motor torque. Then, these currents are separated into positive i_{j+} and negative i_{j-} half-cycles as follows:

$$i_{j+} = \text{pos}(i'_j) = \begin{cases} i'_j & \text{if } i'_j > 0 \\ 0 & \text{if } i'_j \leq 0 \end{cases} \tag{15}$$

$$i_{j-} = \text{neg}(i'_j) = \begin{cases} |i'_j| & \text{if } i'_j < 0 \\ 0 & \text{if } i'_j \geq 0 \end{cases}$$

and the average moving value is then calculated for each one based on the electrical angle,
$hat\rho_e$, as $\bar{i}_{j+}$ and $\bar{i}_{j-}$. Then, the logic signals are defined as:

$$\mathbf{F}_{S_{jk}} = \begin{cases} 0 & \text{if } |\bar{i}_{jk}| \geq S_{th} \\ 1 & \text{if } |\bar{i}_{jk}| < S_{th} \end{cases} \tag{16}$$

where, $\mathbf{F}_{S_{jk}} = [F_{S_{a+}} F_{S_{a-}} F_{S_{b+}} F_{S_{b-}} F_{S_{c+}} F_{S_{c-}}]^T$, the subscript $k \in \{+, -\}$ and S_{th} is a threshold level. This threshold level is obtained as 10% of the average value during normal operation under the rated condition.

It is worth mentioning that when an inverter switch fault occurs, the phase voltages supplying the motor differ from the control reference voltages, $\mathbf{u}^*_{\alpha\beta}$, received as inputs by the observers. Therefore, the estimated currents, from O_c (7), do not match the real values of the IM. This causes the current residuals to increase, triggering the logic signals F_{i_a} and F_{i_b}. After this event, the observer O_s (8) receives the values of $\mathbf{u}^*_{\alpha\beta}$, $\hat{i}_a$ and $\hat{i}_b$ due to the control reconfiguration, leading it to estimate the states perceived by the current observer O_c (see Fig. 2), which prevents the activation of F_ω.

Then, from the obtained logic signals $\mathbf{F}_x$ and $\mathbf{F}_{S_{jk}}$, the FDI stage generates a diagnosis, as explained in the following section.

3.5. FDI

The FDI is based on the Algorithm 1.

Algorithm 1 Proposed sensors reconfiguration and FDI algorithms

Inputs: Currents $\mathbf{i}_{ab}$, speed ω_m
Process current estimation observer O_c (6)
Perform current sensors residuals post-processing (Fig. 3)
Select current sensors feedback according to F_{i_a}, F_{i_b}, and Table 1, assuming $F_w = 0$
Process speed estimation observer O_s (7)
Perform speed sensor residual post-processing (Fig. 3)
Select speed sensor feedback according to F_w, F_{i_a}, F_{i_b} and Table 1
Perform current signals post-processing (Fig. 4)
if $F_w = 1$ **then**
    Diagnosis: Speed sensor fault
else
    if $(F_{i_a} = 1)$ **and** $(F_{i_b} = 1)$ **then**
        if All $F_{S_{jk}} = 1$ **then**
            Diagnosis: Multiple current sensors fault
        else
            Diagnosis: Inverter fault, identify faulty switch based on Table 2
        end if
    else if $F_{i_a} = 1$ **then**
        Diagnosis: i_a sensor fault
    else if $F_{i_b} = 1$ **then**
        Diagnosis: i_b sensor fault
    else
        Diagnosis: Normal operation
    end if
end if
Outputs: selected feedback currents $\mathbf{i}'_{ab}$, selected feedback speed ω'_m, $\hat{\rho}$, fault diagnosis

Once the fault signals $\mathbf{F}_x$ and $\mathbf{F}_{jk}$ are generated, F_ω is evaluated. If active, a speed sensor fault is reported.

Table 2: Switch logic signals

$F_{S_{a+}}$	$F_{S_{a-}}$	$F_{S_{b+}}$	$F_{S_{b-}}$	$F_{S_{c+}}$	$F_{S_{c-}}$	**Diagnosis**
0	0	0	0	0	0	No faults
1	0	0	0	0	0	S_{a+}
0	1	0	0	0	0	S_{a-}
0	0	1	0	0	0	S_{b+}
0	0	0	1	0	0	S_{b-}
0	0	0	0	1	0	S_{c+}
0	0	0	0	0	1	S_{c-}
1	0	0	1	0	0	$S_{a+}\ S_{b-}$
1	0	0	0	0	1	$S_{a+}\ S_{c-}$
0	1	1	0	0	0	$S_{a-}\ S_{b+}$
0	0	1	0	0	1	$S_{b+}\ S_{c-}$
0	1	0	0	1	0	$S_{a-}\ S_{c+}$
0	0	0	1	0	1	$S_{b-}\ S_{c+}$
1	1	0	0	0	0	$S_{a+}\ S_{a-}$
0	0	1	1	0	0	$S_{b+}\ S_{b-}$
0	0	0	0	1	1	$S_{c+}\ S_{c-}$
1	0	1	0	0	1	$S_{a+}\ S_{b+}$
1	0	0	1	1	0	$S_{a+}\ S_{c+}$
0	1	1	0	1	0	$S_{b+}\ S_{c+}$
0	1	0	1	1	0	$S_{a-}\ S_{b-}$
0	1	1	0	0	1	$S_{a-}\ S_{c-}$
1	0	0	1	0	1	$S_{b-}\ S_{c-}$
1	1	1	1	1	1	Current sensors

Otherwise, if both F_{i_a} and F_{i_b} are active, the FDI determines whether the fault occurred in the switches or the current sensors. During this process, it is verified whether all the logic signals of the switches are activated, indicating that $F_{S_{jk}} = 1$. If affirmative, this confirms a simultaneous failure of the current sensors. Note that this condition is analyzed considering only current-sensor disconnection faults. Further research is required to extend the isolation capability to other types of sensor faults. If this condition is not met, it implies that the fault corresponds to one of the inverter switches. Therefore, Table 2 is checked to isolate the faulty switches. Finally, if only one of the fault signals F_{i_a} or F_{i_b} is active, a single current fault is reported in the corresponding sensor.

It is worth mentioning that the fault signals $\mathbf{F}_x$ are also used in the control reconfiguration stage to replace the affected measurements with the corresponding estimates as described in Section 3.2.

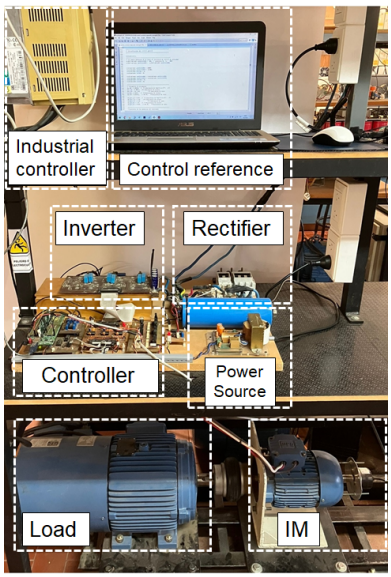

Figure 5: Test-bench.

Table 3: Induction motor parameters

Power	0.75 kW		
Frequency	50 Hz		
Line voltage	26.4 V		
Nominal speed	1435 RPM		
R_s	69.7 mΩ	R_r	34.71 mΩ
L_s, L_r	0.11 mH	L_m	2.66 mH
P	2	J	0.002 94 kgm^2

4. Experimental Validation

The experimental test bench used to validate the proposed strategy is shown in Fig. 5. This test bench is powered by the grid through a rectifier, which in turn feeds an inverter. The inverter is connected to a low voltage IM which is coupled to a second IM used as a load and driven by an industrial controller. The low voltage IM parameters are listed in Table 3. A Texas Instruments TMS320F28335 DSP controller was used to implement the speed control and the FDI strategy, signal acquisition and SVPWM with a switching frequency of 10 kHz. Sensor and OC faults were implemented by forcing the measured signal to zero in the control (sensor disconnection fault) and by deactivating transistor switching signals, respectively, during computer debugging.

The proposed FDI strategy, comprising the two state observers (implemented via numerical integration using Heun's method), residual generation, post-processing

and fault-signal generation, was implemented using a sampling rate of 10 kSPS. The maximum execution time of the complete strategy was 24.6 µs, which represents approximately 25% of the sampling time.

With the described configuration, tests presented below were carried out under different operating points:

- Single and multiple current sensor faults.
- Current sensor fault followed by a speed sensor fault.
- Fault in the inverter switches S_{b+} and S_{b-}.
- Fault in the inverter switches S_{b-} and S_{c-}.

In addition, robustness against speed and torque variations and noise was also analyzed. The following sections describe the obtained results.

4.1. Performance of the FDI strategy under current sensor faults

A consecutive current sensors fault test was conducted, as shown in Fig. 6, with the IM running at a speed of 0.5 pu and with a load torque of 0.5 pu, see Fig. 6(a). A disconnection fault occurs in the i_b sensor at $t = 0.02$ s, followed by a disconnection fault in the i_a sensor at $t = 0.1$ s, as shown in Fig. 6(b), where the three-phase currents are considered, with i_c reconstructed as $i_c = -(i_a + i_b)$. In contrast, Fig. 6(c) presents the estimated currents $\hat{i}_a$ and $\hat{i}_b$, which indicate the expected trajectories of the measured currents. In Fig. 6(a), it can be observed that, despite the faults in sensors i_a and i_b, the difference between ω_m and $\hat{\omega}_m$ is reduced, indicating that the speed sensor diagnosis is not affected. After the fault in i_b, the residual r'_{i_b} (see Fig. 3) exceeds the threshold i_{th} and triggers the fault signal F_{i_b} as shown in Fig. 6(e). In addition, the average measured values $\bar{i}_{b+}$ and $\bar{i}_{b-}$ decrease below S_{th} and produce the activation of $F_{S_{b+}}$ and $F_{S_{b-}}$, see Fig. 6(g). However, the joint activation of F_{i_a} and F_{i_b} does not occur, as the fault is not related to any inverter switch that would consequently affect the current estimates and increase the residuals r'_{i_a} and r'_{i_b}. Then, after the fault in the i_a sensor the residual r'_{i_a} increases above i_{th} and triggers the fault signal F_{i_a}, as can be seen in Fig. 6(d). In addition, the mean values shown in Fig. 6(f) and Fig. 6(h) decrease below S_{th} and the activation of the remaining fault signals occurs which indicates a fault in both current sensors, see Table 2. Based on the results shown, it can be concluded that current sensor faults do not affect the diagnostics of the speed sensor, and that the diagnostics allow for the separation of these faults from those in the inverter switches, as indicated by the $\mathbf{F}_{S_{jk}}$ signals.

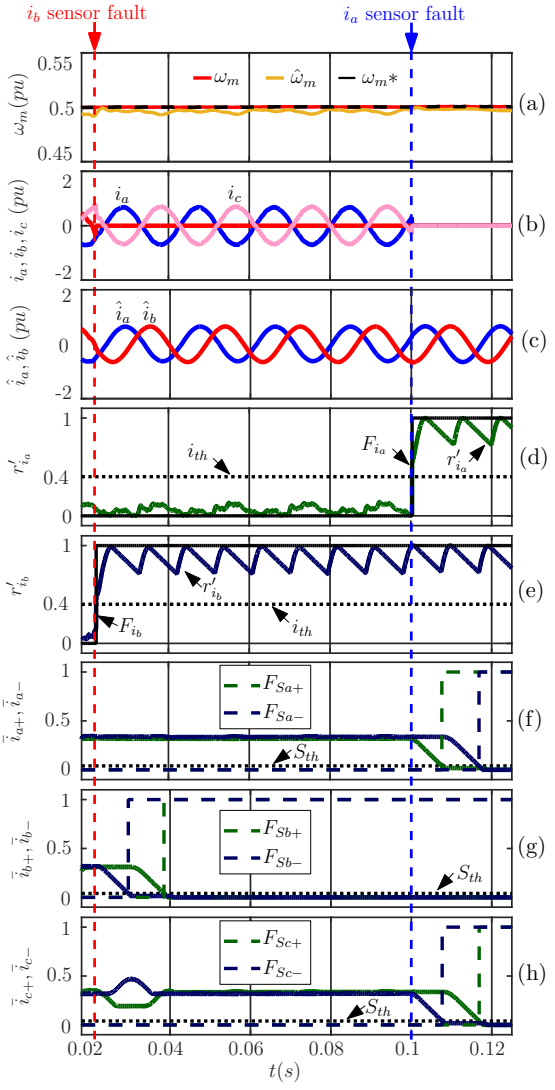

Figure 6: Faults in both current sensors. (a) Measured mechanical speed, ω_m, estimated $\hat{\omega}_m$ and reference ω^*_m. (b) Phase currents i_a, i_b and i_c. (c) Estimated currents $\hat{i}_a$ and $\hat{i}_b$. (d) Phase current residual a, r'_{i_a} and fault signal F_{i_a}. (e) Phase current residual b, r'_{i_b} and fault signal F_{i_b}. (f) Mean value of the positive and negative half cycle of a, and faults signals $F_{S_{a+}}$ and $F_{S_{a-}}$. (g) Mean value of the positive and negative half cycle of b, and faults signals $F_{S_{b+}}$ and $F_{S_{b-}}$. (h) Mean value of the positive and negative half cycle of c, and faults signals $F_{S_{c+}}$ and $F_{S_{c-}}$.

4.2. *Performance of the FDI strategy under current and speed sensor fault.*

In the test shown in Fig. 7 the IM runs at a speed of 0.4 pu with a load torque of 0.5 pu, until $t = 0.04$ s when it accelerates to a speed of 0.63 pu, see Fig. 7(a). Then, a fault occurs in the i_a current sensor in $0.02 \text{ s} < t < 0.57$ s followed by a fault in the speed sensor at $t = 0.09$ s. During the fault of the i_a current sensor (see Fig. 7(c)), the residual r'_{i_a} exceeds the threshold $i_{th} = 0.4$ and activates the fault signal F_{i_a} (see Fig. 7(d)), therefore, the measurement i_a is replaced by the estimation $\hat{i}_a$ of phase current a. This reconfiguration allows, the IMD to remains in operation. Moreover the residual r'_ω is kept at a low level, which avoids a false diagnosis of fault in the speed sensor, see Fig. 2. In addition, at $t = 0.062$ s, the strategy detects that the current sensor has recovered from the fault condition and reconfigures the control replacing $\hat{i}_a$ with i_a.

During the speed sensor fault, the residual r'_ω increases above the threshold $\omega_{th} = 0.4$ and the speed measurement ω_m is replaced by its estimate $\hat{\omega}_m$ to keep running the IMD, see Fig. 7(b). It is worth noting that the residuals r'_{i_a} and r'_{i_b} also increase exceeding the thresholds i_{th}, because the current estimation observer uses the affected speed sensor measurement. Results shown in Figs. 7(d) and (e) show that after the speed sensor fault, the IMD remains in operation. This is because depending on the type of sensor affected, the control replaces the measurement with the corresponding estimate based on the associated diagnosis.

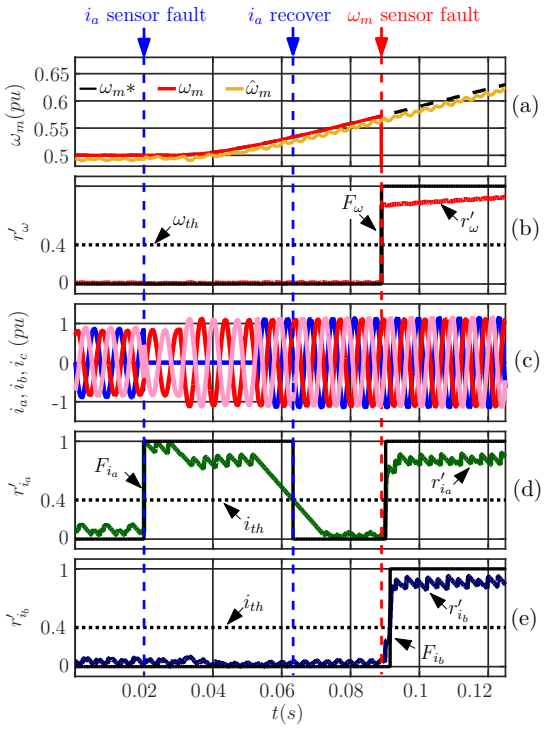

Figure 7: Faults in the ED sensors. (a) Measured mechanical speed, ω_m, estimated $\hat{\omega}_m$, and reference ω^*_m. (b) Speed residual r_ω and fault signal F_ω. (c) Phase currents i_a, i_b e i_c. (d) Phase current residual a, r'_{i_a} and fault signal F_{i_a}. (e) Phase current residual b, r'_{i_b} and fault signal F_{i_b}.

4.3. *Performance of the FDI strategy under OC faults*

Results shown in Fig. 8 were obtained with the IM operating at a speed of 0.75 pu (see Fig. 8(a)) and load torque of 0.7 pu. At $t = 0.03$ s simultaneous OC faults occur on the switches S_{b+} and S_{b-}, therefore, the phase current b becomes null, see Fig. 8(b). This cause the increase of the residual r'_{i_b}, which exceeds the threshold i_{th} and produces the activation of the fault signal F_{i_b} at $t = 0.031$ s, see Fig. 8(d). Then, there is a transient in the residual r'_{i_a} until it settles at a value above the threshold i_{th}, causing activation of F_{i_a}, see Fig. 8(c). Finally, Fig. 8(e) shows that after the fault signals $\bar{i}_{b+}$ and $\bar{i}_{b-}$ decrease reaching a value below the threshold S_{th} which causes the activation of $F_{S_{b+}}$ and $F_{S_{b-}}$. According to the Algorithm 1 and the Table 2, the simultaneous activation of F_{i_a} and F_{i_b}, together with the activation of $F_{S_{b+}}$ and $F_{S_{b-}}$, corresponds to the diagnosis of a fault in leg b. Furthermore, the fault detection and location time corresponds to 14 ms (slightly more than half a current cycle). It is worth mentioning that although the mean values corresponding to the phase currents a and c are not shown, it can be deduced from Fig. 8(b) that they remain above the threshold throughout the test.

Finally, the test shown in Fig. 9 was conducted with the IM operating at a speed of 0.5 pu under a load torque of 0.5 pu. At $t = 0.06$ s, faults occur in the switches S_{b-} and S_{c-}, triggering the activation of F_{i_a} at $t = 0.0605$ s and F_{i_b} at $t = 0.062$ s, see Fig. 9(c) and (d). Subsequently, the inverter logic signals are activated in the sequence $F_{S_{b-}}$, $F_{S_{a+}}$, and $F_{S_{c-}}$; see Fig. 9(e), (f) and (g). From the logic signals from the current sensors and the inverter, and following Table 2, it is possible to isolate the fault in switches S_{b-} and S_{c-} corresponds to 15 ms (slightly less than half a current cycle).

Based on the experimental results shown in Fig. 8 and Fig. 9, it can be concluded that the proposed FDI strategy is capable to diagnose faults in the inverter switches and does not lead to false positives.

4.4. *Robustness against torque and speed variations*

A test was performed to analyze the robustness of the FDI strategy against a sudden variation in the load

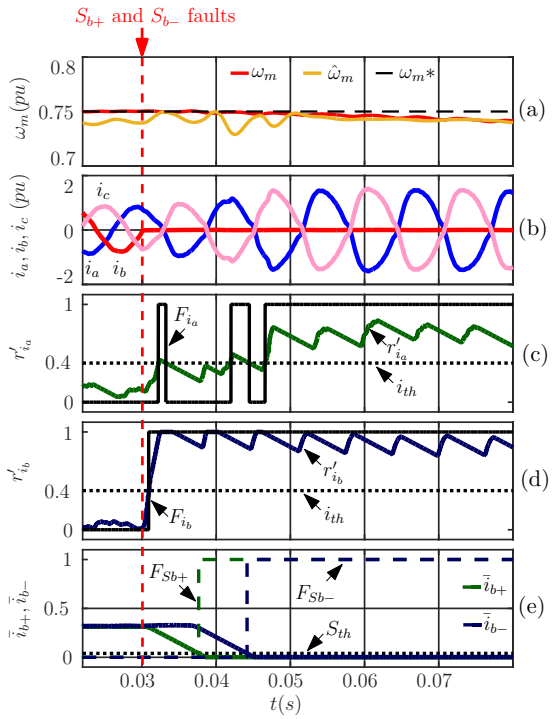

Figure 8: Results including OC faults in S_b^+ and S_b^-. (a) Measured mechanical speed, ω_m, estimated $\hat{\omega}_m$, and reference ω_m^*. (b) Phase currents i_a, i_b e i_c. (c) Phase current residual a, r'_{i_a} and fault signal F_{i_a}. (d) Phase current residual b, r'_{i_b} and fault signal F_{i_b}. (e) Mean value of the positive and negative half cycle of i_b, and faults signals $F_{S_{b+}}$ and $F_{S_{b-}}$.

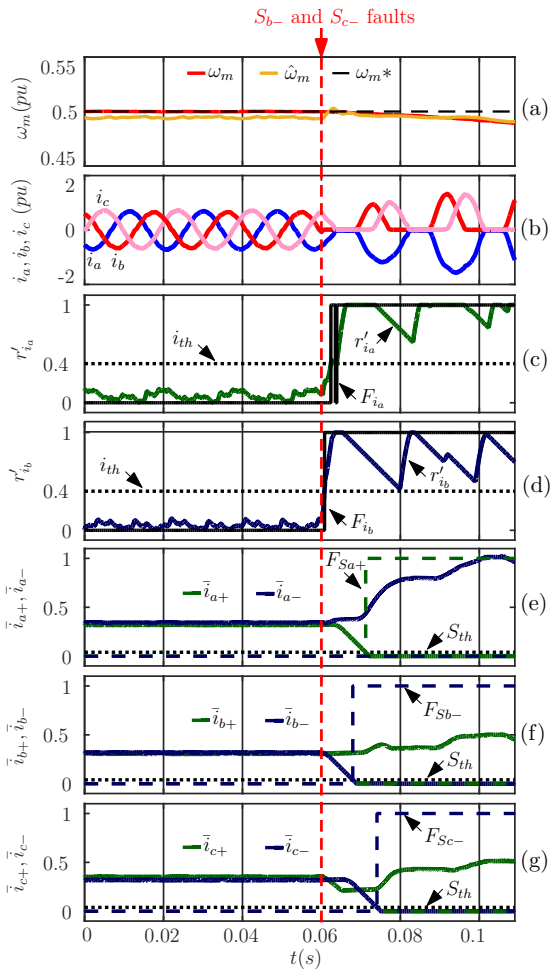

Figure 9: Results including OC faults in S_b^- and S_c^-. (a) Measured mechanical speed, ω_m, estimated $\hat{\omega}_m$, and reference ω_m^*. (b) Phase currents i_a, i_b e i_c. (c) Phase current residual a, r'_{i_a} and fault signal F_{i_a}. (d) Phase current residual b, r'_{i_b} and fault signal F_{i_b}. (e) Mean value of the positive and negative half cycle of i_a, and faults signals $F_{S_{a+}}$ and $F_{S_{a-}}$. (f) Mean value of the positive and negative half cycle of i_b, and faults signals $F_{S_{b+}}$ and $F_{S_{b-}}$. (g) Mean value of the positive and negative half cycle of i_c, and faults signals $F_{S_{c+}}$ and $F_{S_{c-}}$.

torque as shown in Fig. 10. At $t = 0$ s, the IM speed is 0.5 pu and the load torque is 0.3 pu. Then, at $t = 0.1$ s, the load torque is increased to 0.7 pu. As can be seen in Fig. 10(a), the load variation produces a temporary decrease of ω_r until $t = 0.3$ s, when it reaches the reference value. Furthermore, currents peak values increase as a result of the load torque, see Fig. 10(b).

On the other hand, a speed variation test was also performed. The obtained results are shown in Fig. 11 where the IM is operating at a speed of 0.3 pu and the load torque is 0.5 pu at $t = 0$ s. During the time interval 0.1 s < t < 0.5 s, the speed is increased to 0.7 pu. Then, the current peak values increases to 1.15 pu as shown in Fig. 11(b).

It is worth mentioning that in Fig. 10 and Fig. 11, sub-figures (c), (d), and (e) show the residual speed, the maximum value of the current residuals, $r'_{max} = \max(r'_{i_a}, r'_{i_b})$, and the minimum value of the average phase current, $\bar{i}_{min} = \min(\bar{i}_{j+}, \bar{i}_{j-})$, respectively. From the results shown in Fig. 10 and Fig. 11, the values listed in Table 4 were obtained, corresponding to the maximum variation of the index level without a fault and the percentage of the index level relative to the threshold. In conclusion, it can be observed that despite variations in speed and torque, no false positives occur with to the selected threshold levels.

4.5. Robustness against noise

To analyze the robustness against noise, the system of Fig. 1 was simulated using a variable-step Runge-Kutta solver (TR-BDF2) with a fixed 0.1 ms control-loop samplig time and ideal power switches. Several simulations were performed at rated speed, with load torques of 0.5 pu and 0.75 pu, considering different white-noise

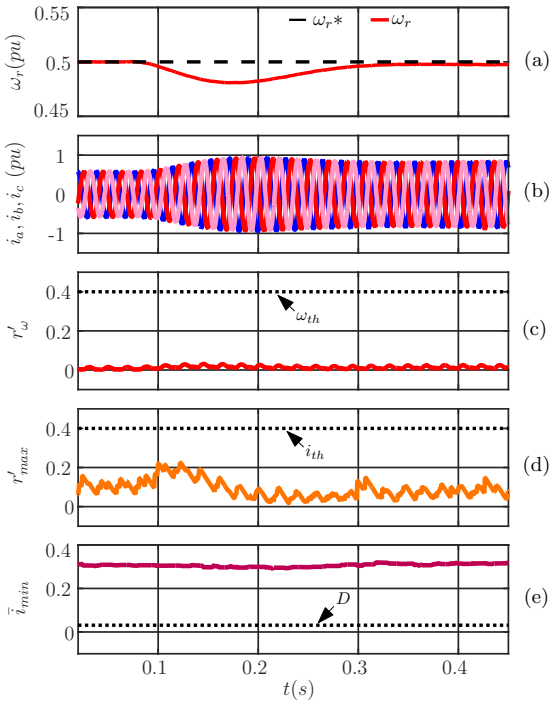

Figure 10: Performance under torque step. (a) Rotor speed, ω_r. (b) Phase currents i_a, i_b, i_c. (c) peed residual r'_ω. (d) Maximum value of phase current residuals. (e) Minimum value of the average phase currents.

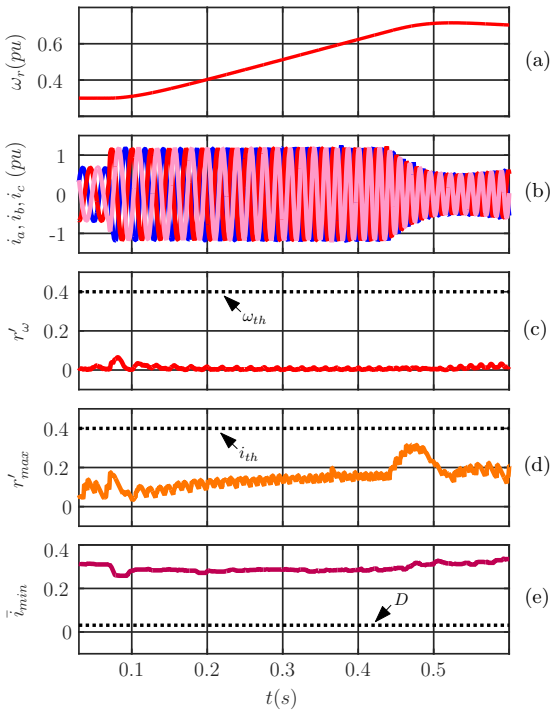

Figure 11: Performance under speed ramp. (a) Rotor speed, ω_r. (b) Phase currents i_a, i_b, i_c. (c) peed residual r'_ω. (d) Maximum value of phase current residuals. (e) Minimum value of the average phase currents.

levels injected in the i_a measurement using the additive fault model (6). The maximum (peak) values of the i_a current, i_b current and speed residuals, denoted by $r^{pk}_{i_a}$, $r^{pk}_{i_b}$, and r^{pk}_{ω}, respectively, were obtained for each noise level, measured as SNR, as shown in Fig. 12. Results indicate that the residual r_{i_a} exceeds its threshold when the SNR is below -0.5 dB (see Fig. 12(a)). In addition, the levels of r_{i_b} and r_ω were not affected by the noise Fig. 12(b). It should be noted that similar results were obtained considering noise in the i_b current measurement. Similarly, Fig. 13 shows the peak residuals $r^{pk}_{i_a}$, $r^{pk}_{i_b}$ (Fig. 13(a)) and r^{pk}_{ω} (Fig. 13(b)) under different noise levels in the speed measurement. In this case, the three residuals were affected by the noise, with residual r_ω exceeding its threshold when the SNR falls below 17 dB.

Note that for an SNR between 20 dB and 30 dB, values considered acceptable for many applications, the residuals remain below their thresholds. It is also important to emphasize that when the SNR falls below this range, these residuals may exceed the thresholds and, consequently, the affected measurements are replaced by their corresponding estimates to ensure the continued operation of the IMD. In many cases, this behavior is expected, since such high noise levels affect the IMD control and should be interpreted as sensor faults.

Table 4: FDI robustness against torque and speed variations

Component	Maximum variation of the index level without fault	% of index level relative to threshold
Current sensor	0.315	78.75
Speed sensor	0.065	16.25
Switch	0.262	15.48

4.6. Comparative performance analysis

The performance of the proposed FDI strategy in detecting different types of faults was evaluated through a comparison with existing strategies for speed and current sensors, as well as inverter switches, with the results summarized in Table 5.

Based on these observations, it can be concluded that the proposed FDI strategy is faster in diagnosing faults in speed and current sensors, requiring only 0.1 ms. This is significantly quicker than the times reported in [18, 30]. It is important to note that, unlike [18], which is limited to single faults in current sensors, and [30], which is also limited to single OC faults

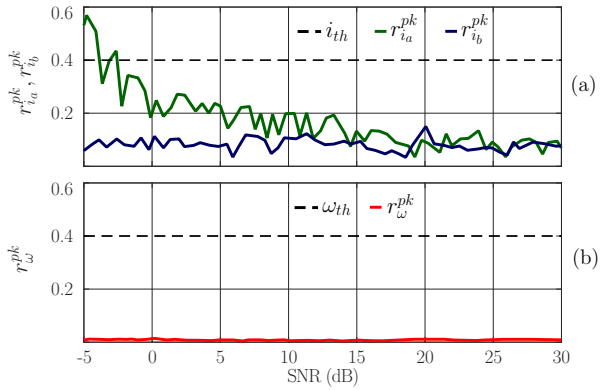

Figure 12: Simulation results considering noise in the measurement of phase current i_a. (a) Phase current residual a, r'_{i_a} and Phase current residual b, r'_{i_b}. (b) Speed residual r'_{ω}.

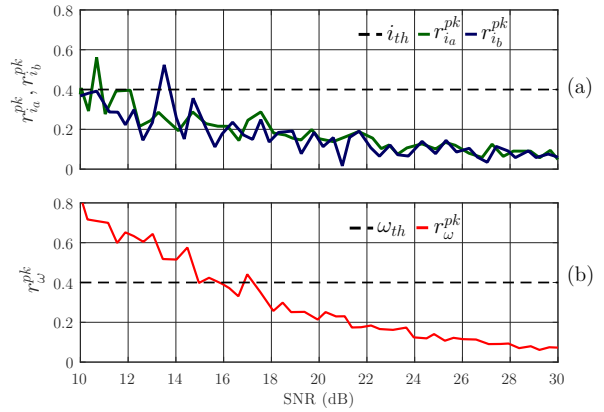

Figure 13: Simulation results considering noise in the measurement of mechanical speed. (a) Phase current residual a, r'_{i_a} and Phase current residual b, r'_{i_b}. (b) Speed residual r'_{ω}.

in inverter switches, the proposed strategy demonstrates the ability to diagnose multiple faults across current sensors. Additionally, it is capable of diagnosing multiple OC faults in inverter switches with a speed nearly as fast as that demonstrated in [18].

5. Conclusion

In this work, a sensor and open-switch fault detection and isolation strategy for induction motor drives (IMD) is proposed and experimentally validated. In addition, a control reconfiguration method is proposed to allow a continuous operation under speed and current sensor faults. This strategy only requires two current sensors and a speed sensor and uses a bank of observers to generate speed and current estimations. A model-based approach is employed for diagnosing sensor faults, while a signal-based analysis is used to diagnosing open-circuit faults in the inverter switches. From the analyzed experimental results, it can be concluded that the proposed strategy is able to identify sensor faults and to perform the control reconfiguration allowing an uninterrupted operation of the IMD. In addition, the strategy is able to detect and isolate open-circuit and differentiate them from faults in the current sensors, which avoids false diagnoses.

Future work will focus on conducting tests under more challenging conditions such as low speeds, as well as refining the isolation algorithm to identify additional types of sensor faults.

Conflict of interest

The authors declare no conflict of interest.

References

[1] C. D. Tran, P. Palacky, M. Kuchar, P. Brandstetter, B. H. Dinh, Current and Speed Sensor Fault Diagnosis Method Applied to Induction Motor Drive, IEEE Access 9 (2021) 38660–38672.

[2] T. X. Nguyen, M. C. H. Nguyen, C. D. Tran, Sensor fault diagnosis technique applied to three-phase induction motor drive, Bulletin of Electrical Engineering and Informatics 11 (6) (2022) 3127–3135.

[3] F. Aguilera, P. M. de la Barrera, C. H. De Angelo, D. E. Trejo, Current-sensor fault detection and isolation for induction-motor drives using a geometric approach, Control Engineering Practice 53 (2016) 35–46.

[4] C. D. Tran, M. Kuchar, V. Sotola, P. D. Nguyen, Fault-Tolerant Control Based on Current Space Vectors against Total Sensor Failures, Sensors 24 (11) (2024) 3558.

[5] K. Hu, Z. Liu, Y. Yang, F. Iannuzzo, F. Blaabjerg, Ensuring a Reliable Operation of Two-Level IGBT-Based Power Converters: A Review of Monitoring and Fault-Tolerant Approaches, IEEE Access 8 (2020) 89988–90022.

[6] U.-M. Choi, F. Blaabjerg, K.-B. Lee, Study and Handling Methods of Power IGBT Module Failures in Power Electronic Converter Systems, IEEE Transactions on Power Electronics 30 (5) (2015) 2517–2533.

[7] X. Zhou, J. Sun, P. Cui, Y. Lu, M. Lu, Y. Yu, A Fast and Robust Open-Switch Fault Diagnosis Method for Variable-Speed PMSM System, IEEE Transactions on Power Electronics 36 (3) (2021) 2598–2610.

[8] H. Tao, T. Peng, C. Yang, J. Gao, C. Yang, W. Gui, Voltage and Current Sensor Fault Diagnosis Method for Traction Converter with Two Stator Current Sensors, Sensors 22 (6) (2022) 2355.

Table 5: Comparison of strategies in terms of FDI time

Component	Proposed FDI	[18]	[30]
Current sensor	0.1 ms	0.874 ms	2 ms
Speed sensor	0.1 ms	< 2 ms	full-cycle
Switch	half-cycle	< half-cycle	full-cycle

[9] F. Aguilera, P. M. de la Barrera, C. H. De Angelo, Speed and current sensor fault-tolerant induction motor drive for electric vehicles based on virtual sensors, Electrical Engineering 104 (5) (2022) 3157–3171.

[10] M. Doostmohammadian, H. Zarrabi, T. Charalambous, Sensor fault detection and isolation via networked estimation: rank-deficient dynamical systems, International Journal of Control 96 (11) (2023) 2853–2870.

[11] X. Sun, N. Diao, C. Song, Y. Qiu, X. Zhao, An Open-Circuit Fault Diagnosis Method Based on Adjacent Trend Line Relationship of Current Vector Trajectory for Motor Drive Inverter, Machines 11 (10) (2023) 928.

[12] T. Orlowska-Kowalska, M. Wolkiewicz, P. Pietrzak, M. Skowron, P. Ewert, G. Tarchala, M. Krzysztofiak, C. T. Kowalski, Fault diagnosis and fault-tolerant control of PMSM drives–state of the art and future challenges, IEEE Access 10 (2022) 59979–60024.

[13] Y. Du, C. Li, Z. Zheng, An Online Metric Learning-Based Open-Switch and Current Sensor Fault Diagnosis for MSPMSM Systems, IEEE Transactions on Power Electronics 38 (7) (2023) 8966–8976.

[14] F. Lu, Q. Guo, Z. Dou, Y. Chen, Q. Wang, X. An, H. Dou, A Novel Simultaneous Diagnosis Method for IGBT Open-Circuit Faults and Current Sensor Faults of Three-Phase SPWM Inverter, IEEE Transactions on Power Electronics (2025).

[15] B. Gou, Y. Xu, Y. Xia, Q. Deng, X. Ge, An Online Data-Driven Method for Simultaneous Diagnosis of IGBT and Current Sensor Fault of Three-Phase PWM Inverter in Induction Motor Drives, IEEE Transactions on Power Electronics 35 (12) (2020) 13281–13294.

[16] L. Xiao, L. Zhang, Z. Yan, Y. Li, X. Su, W. Song, Diagnosis and distinguishment of open-switch and current sensor faults in PMSM drives using improved regularized extreme learning machine, Mechanical Systems and Signal Processing 171 (2022) 108866.

[17] S. K. El Khil, I. Jlassi, A. J. M. Cardoso, J. O. Estima, N. Mrabet-Bellaaj, Diagnosis of Open-Switch and Current Sensor Faults in PMSM Drives Through Stator Current Analysis, IEEE Transactions on Industry Applications 55 (6) (2019) 5925–5937.

[18] I. Jlassi, A. J. M. Cardoso, A Single Method for Multiple IGBT, Current, and Speed Sensor Faults Diagnosis in Regenerative PMSM Drives, IEEE Journal of Emerging and Selected Topics in Power Electronics 8 (3) (2020) 2583–2599.

[19] Y. Sun, J. Chen, R. Qiu, C. Li, Open-Circuit, Current Sensor Fault Diagnosis of Three-Phase Four-Wire Inverters Based on Fourier Fitting, IEEE Transactions on Instrumentation and Measurement 73 (2024).

[20] Z. Li, P. Wheeler, A. Watson, A. Costabeber, B. Wang, Y. Ren, Z. Bai, H. Ma, A Fast Diagnosis Method for Both IGBT Faults and Current Sensor Faults in Grid-Tied Three-Phase Inverters with Two Current Sensors, IEEE Transactions on Power Electronics 35 (5) (2020) 5267–5278.

[21] H. Dan, W. Yue, W. Xiong, Y. Liu, M. Su, Y. Sun, Open-Switch and Current Sensor Fault Diagnosis Strategy for Matrix Converter-Based PMSM Drive System, IEEE Transactions on Transportation Electrification 8 (1) (2022) 875–885.

[22] L. E. Venghi, F. Aguilera, P. M. de la Barrera, C. H. De Angelo, Detection and Isolation of Current-Sensor and Open-Switch Faults in Electric Traction Drives, IEEE Latin America Transactions 19 (8) (2021) 1335–1346.

[23] I. Jlassi, J. O. Estima, S. K. El Khil, N. M. Bellaaj, A. J. M. Cardoso, A Robust Observer-Based Method for IGBTs and Current Sensors Fault Diagnosis in Voltage-Source Inverters of PMSM Drives, IEEE Transactions on Industry Applications 53 (3) (2017) 2894–2905.

[24] S. Xu, X. Chen, F. Liu, H. Wang, Y. Chai, W. X. Zheng, H. Chen, A Novel Adaptive SMO-Based Simultaneous Diagnosis Method for IGBT Open-Circuit Faults and Current Sensor Incipient Faults of Inverters in PMSM Drives for Electric Vehicles, IEEE transactions on instrumentation and measurement 72 (2023).

[25] S. Xu, W. Huang, D. Huang, H. Chen, Y. Chai, M. Ma, W. X. Zheng, A Reduced-Order Observer-Based Method for Simultaneous Diagnosis of Open-Switch and Current Sensor Faults of a Grid-Tied NPC Inverter, IEEE Transactions on Power Electronics 38 (7) (2023) 9019–9032.

[26] S. Xu, W. Huang, H. Wang, W. Zheng, J. Wang, Y. Chai, M. Ma, A Simultaneous Diagnosis Method for Power Switch and Current Sensor Faults in Grid-Connected Three-Level NPC Inverters, IEEE Transactions on Power Electronics 38 (1) (2023) 1104–1118.

[27] S. Xu, H. Yu, H. Wang, H. Chai, M. Ma, H. Chen, W. X. Zheng, Simultaneous diagnosis of open-switch and current sensor faults of inverters in IM drives through reduced-order interval observer, IEEE Transactions on Industrial Electronics (2025).

[28] H. Tao, T. Peng, C. Yang, J. Gao, Z. Chen, C. Yang, W. Gui, An FCS-MPC-based open-circuit and current sensor fault diagnosis method for traction inverters with two current sensors, International Journal of Electrical Power & Energy Systems 144 (2023) 108526.

[29] M. A. Yahiaoui, M. Kinnaert, J. Gyselinck, Augmented State Observer-based Diagnostics of Open-Circuit and Sensor Faults in DFIG Wind Turbines, IEEE Transactions on Power Electronics 38 (12) (2023) 16085–16099.

[30] X. Wang, Z. Wang, Z. Xu, M. Cheng, W. Wang, Y. Hu, Comprehensive Diagnosis and Tolerance Strategies for Electrical Faults and Sensor Faults in Dual Three-Phase PMSM Drives, IEEE Transactions on Power Electronics 34 (7) (2019) 6669–6684.

[31] A. Mohammadi, M. Krysander, D. Jung, Consistency-based diagnosis using data-driven residuals and limited training data, Control Engineering Practice 159 (2025) 106283.

[32] A. Gouichiche, A. Safa, A. Chibani, M. Tadjine, Global fault-tolerant control approach for vector control of an induction motor, International Transactions on Electrical Energy Systems 30 (8) (2020) e12440.

[33] P. Krause, O. Wasynczuk, S. Sudhoff, S. Pekarek, Analysis of Electric Machinery and Drive Systems, IEEE Press Series on Power and Energy Systems, Wiley, 2013.

[34] S. Xepapas, A. Kaletsanos, F. Xepapas, S. Manias, Sliding-mode observer for speed-sensorless induction motor drives, IEE Proceedings-Control Theory and Applications 150 (6) (2003) 611–617.

[35] L. E. Venghi, F. Aguilera, P. M. de la Barrera, C. H. De Angelo, Single-Observer Based Current Sensor Fault Tolerant Control for IM Traction Drives, IEEE Latin America Transactions 19 (12) (2021) 2087–2096.

[36] L. E. Venghi, F. Aguilera, G. N. Gonzalez, P. M. de la Barrera, C. H. De Angelo, Effects of open-switch faults over speed sensor fault-tolerant scheme for electric traction drive, in: 2020 IEEE International Conference on Industrial Technology (ICIT), IEEE, 2020, pp. 731–736.